Energy & Environmental Science

ROYAL SOCIETY OF CHEMISTRY

PAPER

View Article Online
View Journal | View Issue

Cite this: *Energy Environ. Sci.*, 2024, **17**, 3807

Multi-angle tracking synthetic kinetics of phase evolution in Li-rich Mn-based cathodes†

Shenyang Xu, [a] Zhefeng Chen,[a] Wenguang Zhao,[a] Wenju Ren,[ab] Chenxin Hou,[a] Jiajie Liu,[a] Wu Wang,[c] Chong Yin,[d] Xinghua Tan,[a] Xiaobing Lou, [e] Xiangming Yao,[a] Zhihai Gao,[a] Hao Liu,[f] Lu Wang,[a] Zuwei Yin, [a] Bao Qiu, [g] Bingwen Hu, *[e] Tianyi Li, *[h] Cheng Dong, [a] Feng Pan *[a] and Mingjian Zhang*[i]

Received 5th December 2023,
Accepted 8th April 2024

DOI: 10.1039/d3ee04199a

rsc.li/ees

As commercial cathodes with the highest practical capacity, the structural nature of Li-rich Mn-based (LMR) cathodes, composite or solid solution, is still under debate. Due to the extreme structural similarity of two layered-phase components, namely, the monoclinic phase ($C2/m$) and rhombohedral phase ($R\bar{3}m$), no single tool can resolve this concern alone. Herein, we combined multiple advanced techniques to comprehensively study the structural changes during synthesis of LMR cathodes from different aspects such as the elemental distribution, local structure, long-range structure, and short-range structure, revealing a clear process from the formation of two phases to the gradual phase fusion and eventually to a nearly solid solution. Particularly, X-ray pair distribution function (PDF) analysis combined with theoretical simulations reveals for the first time that the transition metal (TM)–TM distance increases with the progress of the phase fusion, which makes the short-range structural change in TM–TM atomic pairs an effective parameter for judging the extent of phase fusion. Eventually, excellent electrochemical performance was achieved by balancing capacity and cycling stability through adjusting the phase fusion to a medium extent in lithium and sodium two layered-phase components. This study establishes an approach to investigate the structural evolution in the complicated multiple-phase system and provides valuable insights into the design and optimization of cathodes by tuning the phase fusion extent.

Broader context

A Li-rich Mn-based (LMR) cathode owns the highest practical capacity among all commercial cathodes, but its structural nature (composite or solid solution) is still under debate, due to the extreme structural similarity of two layered-phase components, namely, the monoclinic phase ($C2/m$) and rhombohedral phase ($R\bar{3}m$). Herein, we combined multiple advanced techniques to comprehensively study the structural changes during synthesis of LMR cathodes from different aspects such as the elemental distribution, local structure, long-range structure, and short-range structure, revealing a clear process from the formation of two phases to the gradual phase fusion and eventually to a nearly solid solution. Particularly, X-ray pair distribution function (PDF) analysis combined with theoretical simulations reveals for the first time that the transition metal (TM)–TM distance increases with the progress of the phase fusion, which makes the short-range structural change in TM–TM atomic pairs an effective parameter for judging the extent of phase fusion. Eventually, excellent electrochemical performance was achieved in LMR cathodes through adjusting the phase fusion extent, and the strategy was further validated in another P2–O3 bi-phase complex cathode for Na-ion batteries. This work represents a significant stride in cathode technology and methodology for analyzing complicated multi-phase systems.

[a] *School of Advanced Materials, Shenzhen Graduate School, Peking University, Shenzhen 518055, China. E-mail: panfeng@pkusz.edu.cn*
[b] *School of Advanced Manufacturing Engineering, Chongqing University of Posts and Telecommunications, Chongqing 400065, China*
[c] *Shenzhen Key Laboratory of Thermoelectric Materials, Department of Physics, Southern University of Science and Technology, Shenzhen 518055, China*
[d] *Ningbo Ronbay Lithium Battery Material Co., Ltd, Ningbo 315400, China. E-mail: bwhu@phy.ecnu.edu.cn*
[e] *Shanghai Key Laboratory of Magnetic Resonance, State Key Laboratory of Precision Spectroscopy, School of Physics and Electronic Science, East China Normal University, Shanghai 200241, China*
[f] *Institute for Applied Materials, Karlsruhe Institute of Technology, Hermann-von-Helmholtz-Platz 1, Eggenstein-Leopoldshafen 76344, Germany*
[g] *Ningbo Institute of Materials Technology and Engineering, Chinese Academy of Sciences, Ningbo 315201, China*
[h] *Chemical Sciences and Engineering Division, Argonne National Laboratory, Lemont, IL 60439, USA. E-mail: tianyi.li@anl.gov*
[i] *School of Science and Engineering, The Chinese University of Hong Kong, Shenzhen, Guangdong 518172, China. E-mail: zhangmingjian@cuhk.edu.cn*

† Electronic supplementary information (ESI) available. See DOI: https://doi.org/10.1039/d3ee04199a

Introduction

Li-rich Mn-based materials (LMRs), $x\mathrm{Li}[\mathrm{Li}_{1/3}\mathrm{Mn}_{2/3}]\mathrm{O}_2\cdot(1-x)\mathrm{LiTMO}_2$ (TM = Ni, Co, Mn), are some of the most promising candidates for next-generation cathodes with high energy density.[1–5] Nevertheless, the complicated elemental composition and phase structures of LMRs, which involves four metal elements and diverse cation arrangements, pose substantial challenges in controlling the synthesis process and ensuring consistent electrochemical performance. Furthermore, there is a long-standing debate regarding the LMR phase structure. Some studies propose a composite made up of two layered phases, namely, $\mathrm{Li}_2\mathrm{MnO}_3$ (S. G. $C2/m$) and LiTMO_2 (S. G. $R\bar{3}m$),[6–11] while others suggest a solid solution of two phases.[12,13] Actually, the real structure depends greatly on the synthetic conditions, and different temperatures, times, and heating/ cooling rates would lead to different structures.[14] That is why there are so many different reports on the structure and electrochemistry of LMR cathodes. Therefore, it is essential and crucial to figure out the whole process of phase structure evolution during the synthesis of LMR cathodes, which can end the long-standing controversy and benefit the controllable and precise synthesis of so complicated a material system.

Our recent study revealed that the lattice strain of the two phases of a LMR is the origin of structural degradation.[15] Nevertheless, the two compositional phases in the LMR are extremely similar, thus posing a great challenge. They have the same O3-type layered structure composed of alternately stacking Li layers and transition metal (TM) layers, and only show tiny differences in the elemental composition and cationic arrangement in TM layers. Element-sensitive transmission electron microscopy (TEM)–energy dispersive X-ray spectroscopy (EDX) can distinguish two layered phases with different TM compositions by probing the elemental distribution, but it fails if the difference in elemental spatial distribution is at the ten-nanometer level.[11,14] X-ray diffraction (XRD) coupled with Rietveld refinement is another powerful technique to identify the long-range phase structure and analyze the phase composition, but it does not work well here since the XRD patterns of two phases nearly overlap with each other, except the superlattice peaks of the monoclinic phase. Local-structure sensitive high-resolution TEM can probe the spatial distribution of two phases, but it works only when taking images along the special direction showing the Li–Mn–Mn···Li–Mn–Mn··· arrangement in TM layers, which is the sole structure feature of the monoclinic phase different from the rhombohedral phase. X-ray total diffraction coupling with pair distribution function (PDF) analysis has the unique capability of analyzing both long-range and short-range structure information, especially the latter part may work to distinguish so similar two phases with tiny local structural differences.[6,12,13] Overall, no single available technique can adequately track the whole phase transition process from the two-phase composite to the solid solution phase due to the respective detection limits in the element and structure.[16–18] In this context, it is required to combine various advanced techniques together for gaining a comprehensive understanding of the structure evolution behavior in LMR cathode materials.

Herein, we perform a systematic investigation of the phase transition during the sol–gel synthesis of LMR cathodes using a combination of advanced techniques, including TEM–EDX, transmission Kikuchi diffraction (TKD), TEM, synchrotron X-ray diffraction (SXRD), PDF analysis, solid-state nuclear magnetic resonance (ssNMR) spectroscopy and theoretical calculations, from multiple aspects such as the elemental distribution, long-range structure, local structure, and short-range atomic ordering (Scheme 1). The whole process is clearly elucidated from the formation of two phases to the gradual phase fusion and eventually to a complete phase fusion. Especially, PDF analysis shows a clear change in the distance of the TM–TM atomic pair with temperature, which can act as an important judgement to track the extent of two-phase fusion. Furthermore, a LMR cathode with a medium extent of phase fusion exhibits excellent cycling stability without sacrificing the capacity due to the unique nanodomain structure. These studies enhance our understanding of the structural nature of LMR

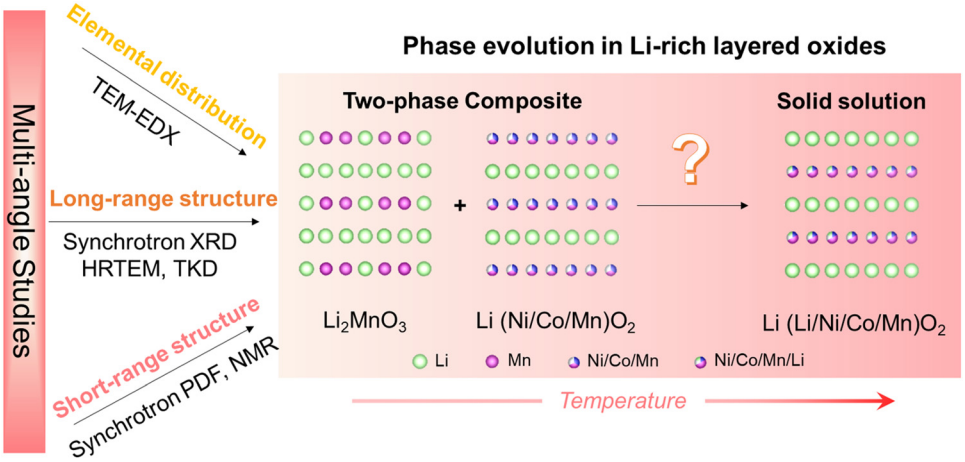

Scheme 1 Schematic illustration of a combination of advanced tools to study the phase structure evolution of LMR cathodes from multiple-angle.

cathodes and provide the possibility of harnessing the full potential of LMR cathodes in practical applications.

Results and discussion

The changes in elemental distribution and local phase structure

Since the formation and interplay of two layered phases are accompanied by TM segregation and interdiffusion during the synthesis of LLNCM, we adopted TEM–EDX to track the changes in elemental distribution with temperature (Fig. 1). As for LLNCM-700 (Fig. 1a and Fig. S3, ESI†), the elemental distribution of Mn, Co, and Ni is not uniform among the primary particles, showing Mn-concentrated particles and Co/Ni-concentrated particles (nearly a core–shell structure). It should correspond to the formation and separation of the two layered phases Li_2MnO_3 (Mn-rich) and $LiNi_{1/3}Co_{1/3}Mn_{1/3}O_2$ (NCM111, Ni/Co rich) in the LMR cathode, since Li_2MnO_3 can be obtained at a lower temperature than NCM111 (Fig. S4, ESI†).[19–21] When the temperature reaches 800 °C and above (Fig. 1b–e), the Mn, Co and Ni distribution becomes uniform at the nanoscale. This indicates that the elemental interdiffusion of Mn, Co and Ni between Li_2MnO_3 particles and NCM111 particles takes place during the further sintering process and is basically completed by 800 °C. This results from the structural similarity of the two phases and confirms the element tolerance of the 3*a* (TM) sites in NCM111 and the 4*g* (Mn) sites in Li_2MnO_3. The results also indicate that TEM–EDX fails to track the further phase fusion process above 800 °C.

To track the phase evolution above 800 °C, HRTEM images are taken at the particle surface and in the bulk of different samples. As shown in Fig. 2a–c and Fig. S5 (ESI†), it is easy to find the phase fusion regions with the clear grain boundary within the individual particles of LLNCM-800, LLNCM-900, and LLNCM-1000. They all present two layered phase domains (Regions 1 and 3 marked in Fig. 2a–c) and the spinel-like region in between (Region 2 marked in Fig. 2a–c). It is hard to identify

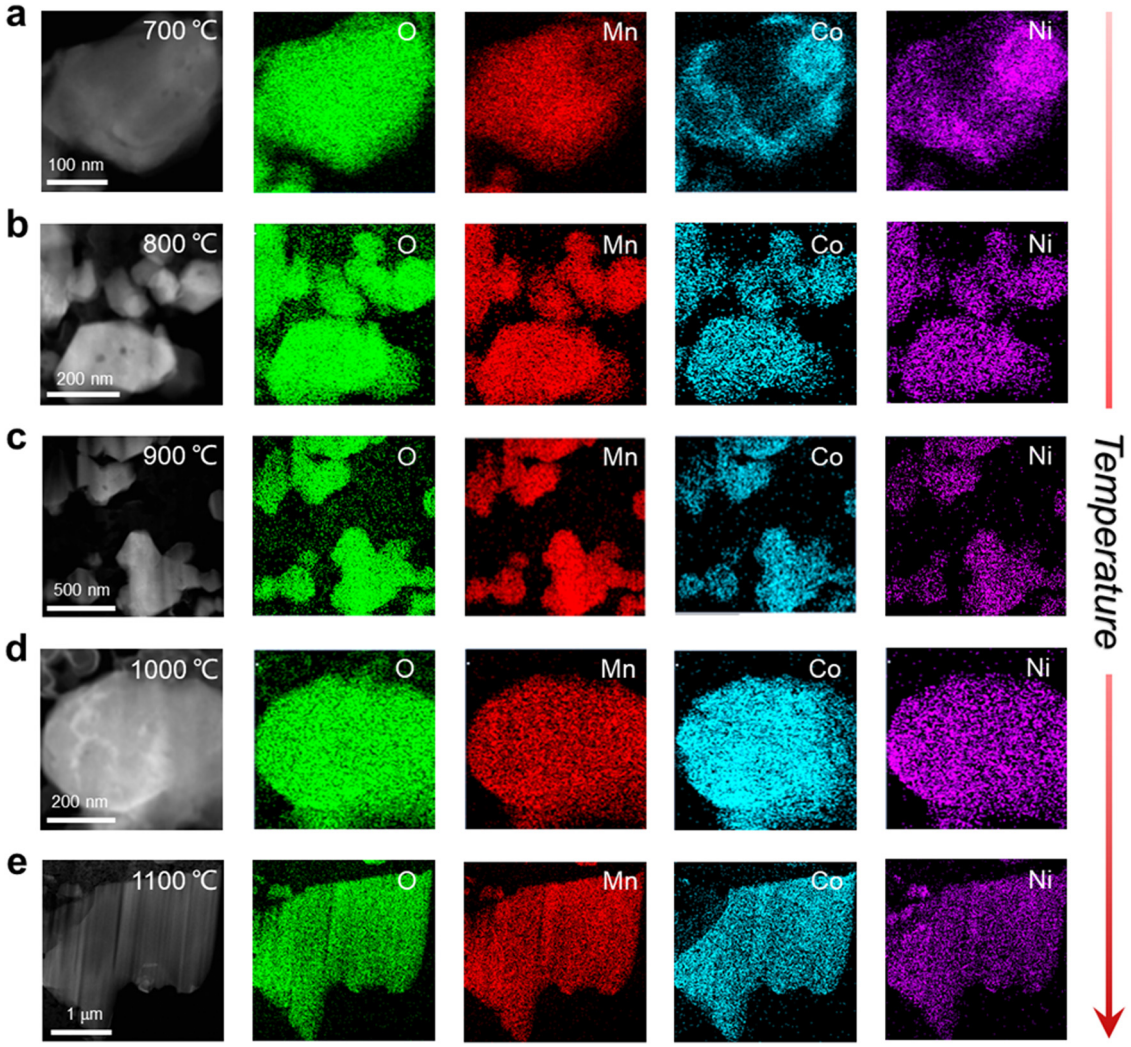

Fig. 1 Elemental interdiffusion kinetics. *Ex situ* TEM images and the corresponding EDX spectra of O, Mn, Co, and Ni for LLNCM-700 (a), LLNCM-800 (b), LLNCM-900 (c), LLNCM-1000 (d) and LLNCM-1100 (e).

two layered phase regions as the monoclinic phase or rhombohedral phase due to the same O3-type arrangement and the similar inter-layer distances. The spinel-like region in between hints that the phase fusion between two layered phases progresses through TM migration and re-arrangement. When the temperature reaches to 1100 °C, we cannot find any grain boundary within single particles. As shown in Fig. 2d, the same layered lattice fringes with the same orientation can be observed in the bulk region (Region 1) and at the particle surface (Region 2). Furthermore, we expand upon the discussion regarding the bulk structure of LLNCM-1000 and LLNCM-1100 by high-angle annular dark field-scanning transmission electron microscopy (HADDF-STEM). As depicted in Fig. S6 (ESI†), LLNCM-1100 exhibits distinct particles. This observation substantiates the conclusion that the grain boundaries within LLNCM-1100 are inter-particle. In Fig. 2e and f, both LLNCM-1000 and LLNCM-1100 exhibit no obvious contrast difference in transition metal layers. Nevertheless, the intensity profile of LLNCM-1000 displays a greater variance in brightness, hinting at a more random arrangement of transition metals in LLNCM-1100. This hypothesis warrants further investigation through analysis of local structural changes. Selected area electron diffraction (SAED) is further performed to analyze the structure at the single particle level. As shown in Fig. S7 (ESI†), it exhibits different crystal directions, demonstrating the polycrystalline character of LLNCM-1000 particles, while LLNCM-1100 particles demonstrate a singular orientation (Fig. S8, ESI†), confirming the single crystal character. These findings are in alignment with the outcomes obtained from TKD analysis (Fig. 2g–i). The TKD tests with the unique capability of identifying the crystal orientation of the nanocrystals with a sub-10 nm spatial resolution[22] were performed on the individual particles of LLNCM-1000 and LLNCM-1100 (Fig. 2g). As shown in Fig. 2h, the projection maps from three different angles for LLNCM-1000 show the separation of two diffraction spots (marked by the arrows). This indicates that

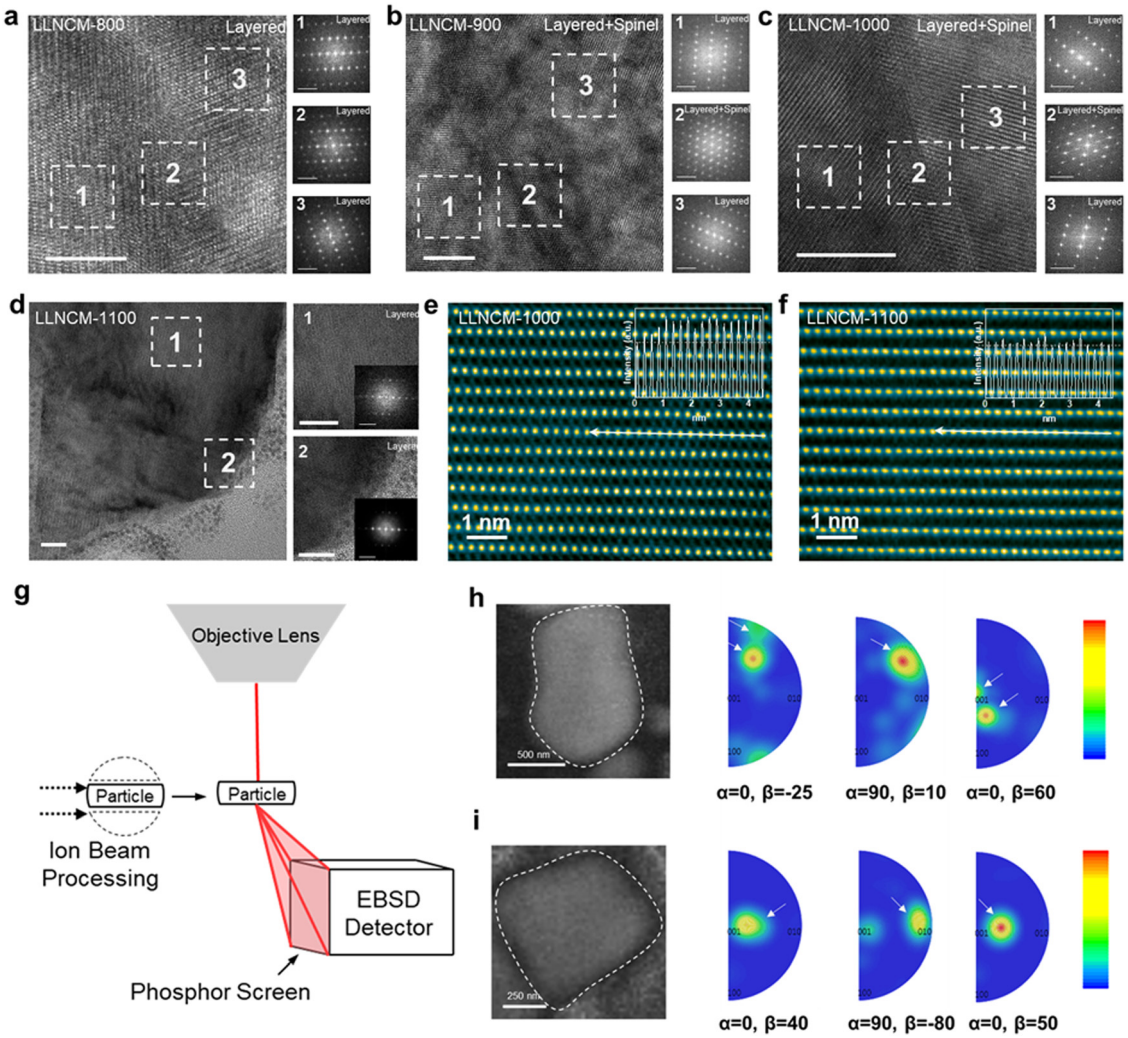

Fig. 2 Microstructural changes with temperature. HRTEM images of LLNCM-800 (a), LLNCM-900 (b), and LLNCM-1000 (c) in the bulk and LLNCM-1100 (d). The FFT maps are deduced from the corresponding regions. The scale bars in HRTEM images and FFT maps are 10 nm and 2 1/nm, respectively. (e) and (f) HADDF-STEM images of LLNCM-1000 and LLNCM-1100. (g) Schematic diagram of the TKD test on the cross-section sample of an individual particle. Inverse pole figures (IPF) and the corresponding images of an LLNCM-1000 particle (h) and an LLNCM-1100 particle (i).

there are different crystal orientations within a single particle, hinting at the polycrystal or twin-crystal nature. Differently, the projection maps from three different angles for LLNCM-1100 (Fig. 2i) show only one diffraction spot, hinting at the single-crystal nature of the individual particle. In brief, HRTEM combined with TDK results indicate that it achieves a relatively high degree of fusion at the nanodomain scale by 1100 °C, but cannot distinguish the different extents of phase fusion from 800 to 1000 °C.

The change in the long-range structure

Li_2MnO_3 and NCM111 have the same O3-type layered structure composed of alternately-stacking Li layers and TM layers, and only show tiny differences in the elemental composition and cationic arrangement in TM layers. As shown in Fig. 3a, TM layers in monoclinic Li_2MnO_3 consist of MnO_6 octahedra interleaved with LiO_6 octahedra. TM layers in rhombohedral $LiTMO_2$ are made up of disordered NiO_6, CoO_6 and MnO_6 octahedra. The simulated XRD patterns of Li_2MnO_3 and $LiTMO_2$ are shown in Fig. S9 and S10 (ESI†). All diffraction peaks of $LiTMO_2$ are basically overlapped with those of Li_2MnO_3. As a powerful tool to identify the phase structure of crystalline materials, SXRD was applied to investigate the phase evolution during the sintering process.[23] Fig. 3b shows the SXRD patterns of LLNCM-700, LLNCM-800, LLNCM-900, LLNCM-1000, and LLNCM-1100. It is clear that the $(003)_R$ and $(104)_R$ peaks of the rhombohedral phase NCM111 are nearly overlapped with the $(001)_M$ and $(131)_M$ peaks of the monoclinic phase Li_2MnO_3, respectively, due to the very close crystal plane spacings with a difference of ~0.01 Å ($d(003)_R$ = 4.7423 Å,

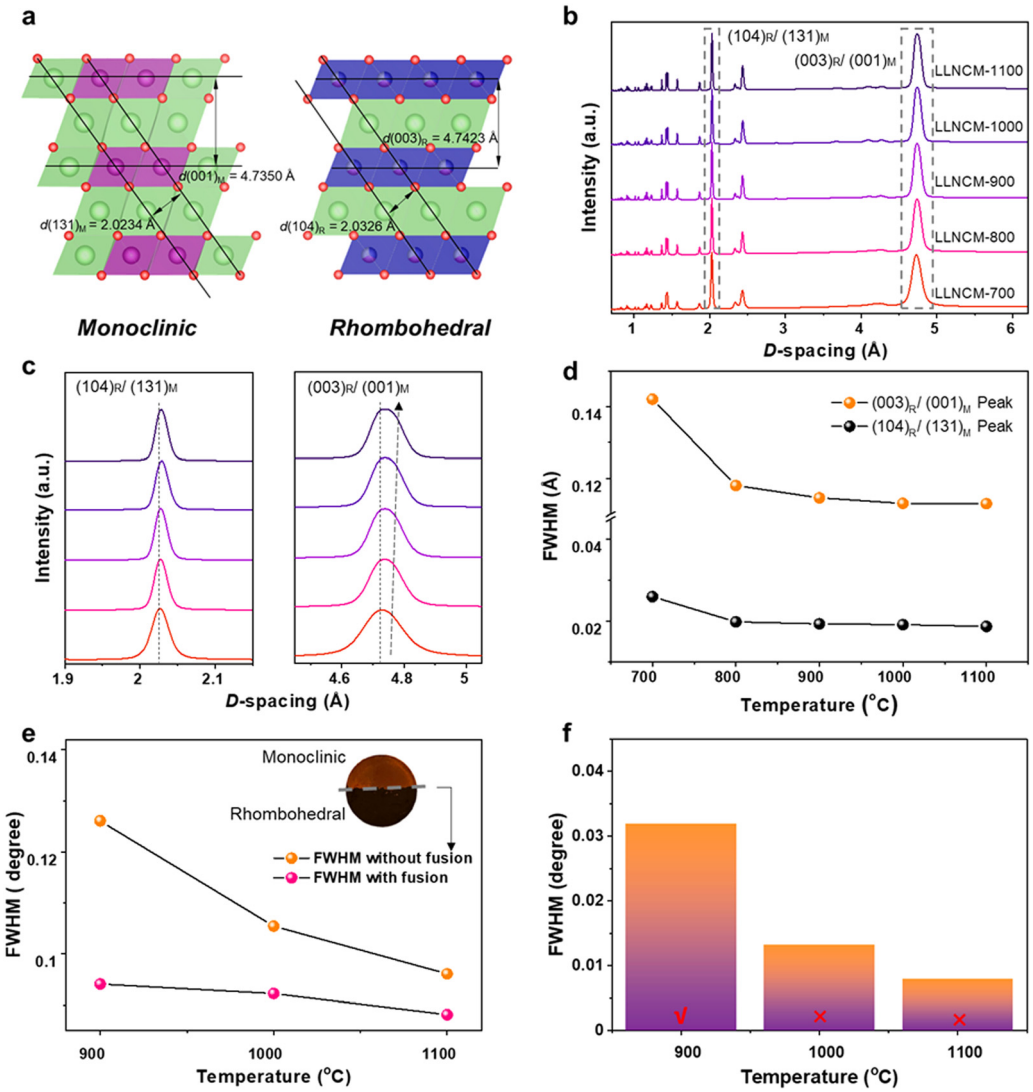

Fig. 3 Long-range structure evolution. (a) The crystal structures of the monoclinic phase and rhombohedral phase with the corresponding crystallographic planes marked. (b) *Ex situ* SXRD patterns of as-prepared Li-rich Mn-based layered oxides LLNCM-700, LLNCM-800, LLNCM-900, LLNCM-1000 and LLNCM-1100. (c) The enlarged $(003)_R/(001)_M$ and $(104)_R/(131)_M$ peaks from (b). (d) The corresponding FWHM values of $(003)_R/(001)_M$ and $(104)_R/(131)_M$ peaks as a function of temperature. (e) $(003)_R/(001)_M$ FWHM values with and without two-phase diffusion at different temperatures and (f) the corresponding differences in FWHM from (e).

$d(104)_R$ = 2.0326 Å, $d(001)_M$ = 4.7350 Å, $d(131)_M$ = 2.0234 Å) (Fig. 3a).

Nevertheless, we can distinguish the two phases a little according to the asymmetric peak shape and the peak shift of the enlarged prominent peaks in Fig. 3c. The $(003)_R/(001)_M$ peak shows a continuous peak shift to the large *D*-spacing direction with temperature (marked by the arrow in Fig. 3c), corresponding to the increase of inter-layer distance. This hints at a phase fusion process from the monoclinic phase to the rhombohedral phase since the rhombohedral phase has a larger interlayer distance than the monoclinic phase. This is consistent with the TEM images in Fig. 1, evidencing progressive phase fusion from the nanoparticle composite to the nanodomain-level interdiffusion.

In addition, it is reasonable that the extent of peak overlap should increase with the gradual two-phase fusion, leading to a decrease of the full width at half maximum (FWHM). Therefore, the FWHM values (Fig. 3d) are plotted as a function of temperature to track the two-phase fusion. The FWHM values of both peaks show a decreasing trend with temperature from 700 °C to 900 °C, hinting at the phase fusion to some extent, since they have similar particle sizes (Fig. S1, S2 and S11, ESI†). Especially, there are huge drops from 700 °C to 800 °C, which corresponds to the change of elemental distribution from non-uniformity to uniformity at the nanoscale level (Fig. 1a and b). This demonstrates a corresponding correlation between phase fusion and elemental diffusion. When the temperature further increases, the changes of the FWHM values above 900 °C are not obvious, hinting that the parameter FWHM hardly reflects the higher extent of phase fusion above 900 °C. And *in situ* heating XRD analyses were performed at 800, 900 and 1000 °C (Fig. S12–S15, ESI†). The results demonstrated that temperature exerted a stronger influence over structural changes of lithium-rich materials than a prolonged heating duration (>5 hours), and the cooling process had minimal effect on the FWHM values. Thus, the capability of X-ray diffraction to discern the nuances of the fusion process at the particle level warrants further investigation.

Rietveld refinement was also performed on *ex situ* SXRD patterns to try to analyze the changes in phase composition (Fig. S16 and S17 and Tables S2–S4, ESI†). As shown in Fig. S17 and Tables S3 and S4 (ESI†), good fitting results with similar R_{wp} values can be obtained even using different phase compositions at 1000 °C. This indicates that Rietveld refinement loses efficacy to track the phase composition when two phases exhibit extremely similar structures. Refinements were further performed using stacking fault models (Fig. S18, ESI†).[24–26] As the temperature increases, the staking fault probability basically shows a decreasing trend (Table S5, ESI†). It is reasonable that the higher phase fusion degree at high temperatures would break up the Li/Mn ordering in the transition metal layer, leading to fewer stacking faults. The increasing temperature will cause a more well-defined atomic arrangement. As a result, the diffraction peaks appear sharper.

Given the challenges associated with employing traditional XRD analysis to monitor fusion at the nanodomain scale, it is imperative to perform specialized experiments aimed at elucidating the fusion process within LLNCM-900, LLNCM-1000, and LLNCM-1100. We decoupled the fusion process by using the same proportion of NCM111 and Li_2MnO_3 materials as the experimental materials, dispersed the cathode of the two-phase structures on both sides to prevent the phase fusion, and conducted XRD testing after adopting the same calcination conditions (illustrated in Fig. 3e, f and Fig. S19, ESI†). Then we strictly designed XRD experiments to exclude the influences of crystallinity and particle size on the FWHM of main peaks (Fig. S20, ESI†). According to Scherrer's formula:

$$\mathrm{FWHM} = \frac{k\lambda}{D_{hkl}\cos\theta_{hkl}}$$

where D_{hkl} is the grain size in the normal direction, k is the shape factor, and λ is the wavelength. We calculated the effect of grain size differences on the FWHM of the $(003)_R/(001)_M$ peaks (Fig. S20, ESI†) and found that when the grain sizes differed by 100 nm, the difference in the half-peak width of XRD measured under the copper target was less than 0.015 degrees. It is clear that the difference in the FWHM value at 900 °C (>0.03 degrees) is much larger than the error (0.015 degrees, which resulted from the effect of grain size on FWHM mentioned above). Accordingly, the difference in FWHM at 900 °C can be used as a criterion for nanodomain diffusion. But when the temperature rises to 1000 °C or beyond, no nanodomain scale diffusion occurs and local structures need to be used for judgment.

Overall, synchrotron XRD is able to track the beginning part of two-phase fusion from the nanoparticle composite to the initial phase fusion within a single particle at the nanodomain scale, but works not so well to probe the higher extent of phase fusion with the TM interdiffusion at the atomic level in individual particles.

The changes in the short-range structure

Based on the results above, the phase fusion above 900 °C is hard to detect since this part only involves Li/TM diffusion and rearrangement in TM layers at the atomic level without changing lattice parameters much. Here synchrotron X-ray total scattering coupling with PDF analysis was employed to detect short-range structural changes, especially the changes of TM coordination environments accompanied by the TM rearrangement. As shown in Fig. S21 (ESI†), the full PDF patterns of five samples present very similar profiles, hinting at similar long-range layered structures. To further examine short-range structural changes, the region in 1.5–3.2 Å is enlarged in Fig. 4a. The peaks around 1.9 and 2.8 Å can be assigned to the TM–O bond and TM–TM atomic pair, respectively. All samples have nearly the same TM–O peak position, indicating that TM–O bond length in TMO_6 octahedra does not change with the phase fusion. The TM–TM peak gradually shifts to the high *r* direction with temperature, especially for LLNCM-1100, indicating a longer average TM–TM distance at 1100 °C (Fig. 4b). The refinement results of PDF patterns are summarized in Fig. S22, Tables S6 and S7 (ESI†). We found that these changes

in the TM–TM peak intensity and position were mainly due to the variations of lattice parameters and oxygen positions. To further investigate the changes in the valence state of the TM and the local structure, X-ray absorption near edge structure (XANES) and extended X-ray absorption fine structure (EXAFS) spectra were collected on both LLNCM-1000 and LLNCM-1100. As shown in Fig. S23 (ESI†), Mn exhibits a decrease in the valence state with temperature, while Ni and Co exhibit an increase in the valence state. This suggests a higher degree of Ni and Co incorporation into the $LiMn_6$ structure.[27–29] The EXAFS spectra of Ni K-edge and Co K-edge exhibit elongated TM–TM distances and diminished intensity for Ni–TM and Co–TM interactions (Fig. S24, ESI†).

The elongation of TM–TM distance may be related to the phase fusion process. In order to validate the deduction, we developed a special quasi-random structure (SQS) system to construct structure models with different fusion degrees – low, medium and high (Fig. 4c and Fig. S25 and S26, ESI†). The low fusion model (initial structure) is composed of alternately stacked TM layers from Li_2MnO_3 (marked by a blue dashed rectangle) and TM layers from NCM111 (marked by an orange dashed rectangle). In the solid solution structure with the maximum degree of phase fusion, Li^+ and the transition metal ions are randomly arranged in TM layers. The system energy increases with the degree of phase fusion (Fig. S27, ESI†). This aligns with the generally accepted principle that greater fusion requires higher energy input. Within these structure models, different coordination environments of Li in TM layers are numbered and counted, and presented in the histogram form

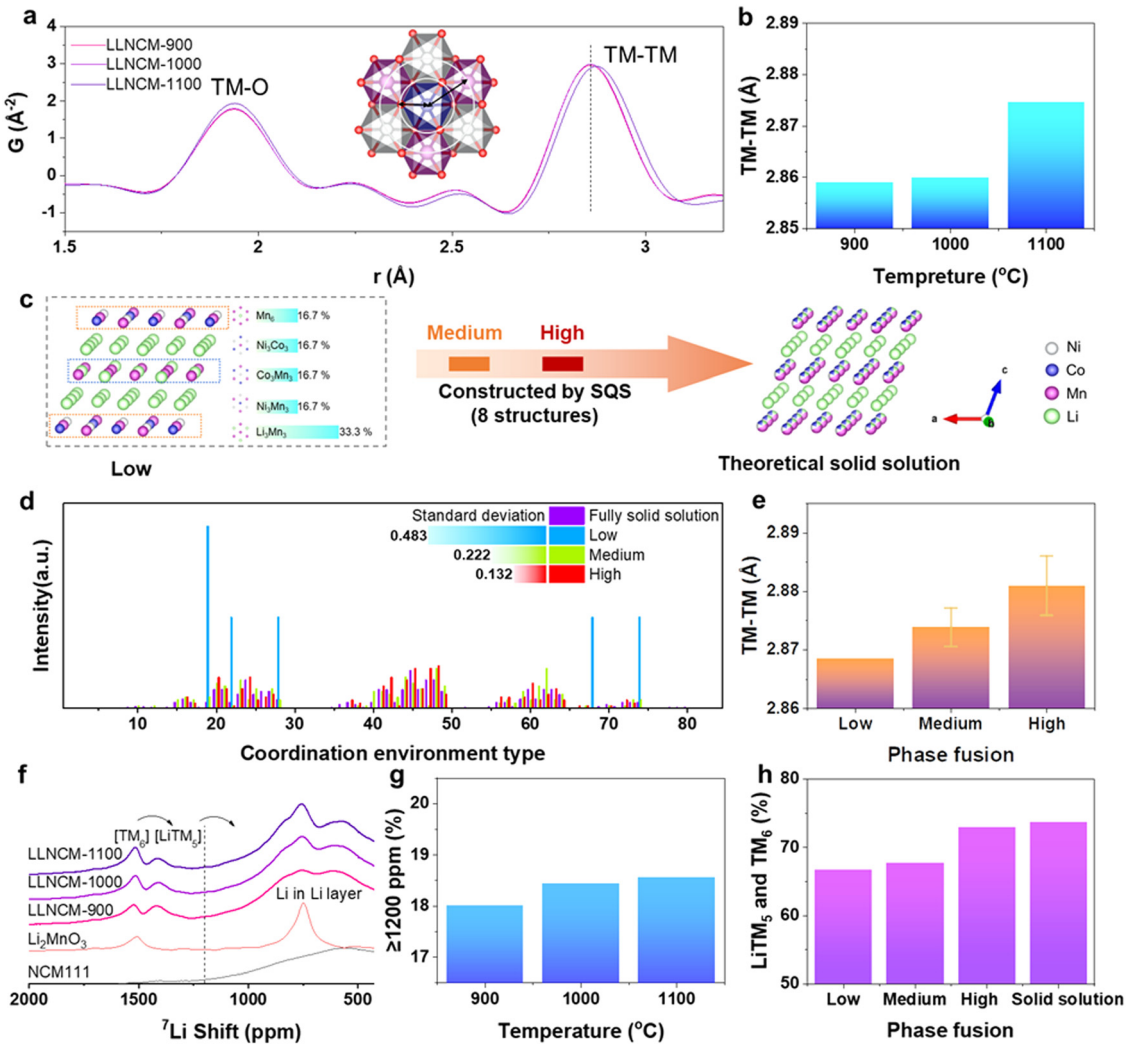

Fig. 4 The short-range structure evolution at the atomic scale. (a) Synchrotron PDF patterns of LLNCM-900, LLNCM-1000 and LLNCM-1100 in the short *r* region of 1.5–3.2 Å. (b) The TM–TM distance as a function of temperature, deduced from (a). (c) Schematic illustration of the construction of structure models with low, medium, and high extents of phase fusion between Li_2MnO_3 and NCM111 phases by the SQS method. SQS means a special quasi-random structure. The structure models with medium and high phase fusion extents are presented in Fig. S25 and S26 (ESI†). (d) The local coordination environment statistics in structure models with low, medium, and high extents of phase fusion. The detailed results are summarized in Tables S8–S10 (ESI†). (e) The calculated TM–TM distance as a function of the extent of phase fusion. (f) Deconvoluted ^{7}Li MAS ssNMR of LLNCM-900, LLNCM-1000, LLNCM-1100, NCM111 and Li_2MnO_3. (g) The area proportions of resonances ≥1200 ppm for LLNCM-900, LLNCM-1000 and LLNCM-1100. (h) Proportions of $LiTM_5$ and TM_6 configurations in transition metal layers as a function of the phase fusion extent based on the model structures.

(Fig. 4d). The standard deviations were calculated using the fully solid solution as the reference, and the values are 0.483, 0.222 and 0.132 for low, medium and high degrees of phase fusion, which is self-consistent and reasonable. We further extracted the TM–TM distances from these structure models and found a positive correlation between TM–TM distance and the phase fusion degree (Fig. 4e), which is highly consistent with the experimental results (Fig. 4b). We can deduce that the change in TM–TM distance arises from the variations in local coordination environments. Combining the PDF results and theoretical calculations, we can conclude that the TM–TM distance can act as an effective parameter to quantify the extent of phase fusion when the samples have identical elemental compositions and are synthesized using the same methodology. A larger TM–TM distance indicates a higher extent of phase fusion. The TM–TM distance of LLNCM-1100 obtained from PDF results is 2.875 Å (Fig. 4b), close to the calculated value (2.88 Å) for the high fusion extent (Fig. 4e). So LLNCM-1100 can be considered to approach the ideal solid solution.

To further confirm the reliability of theoretical calculations, we examined the changes in the Li local environment with temperature by ^{7}Li magic angle spinning (MAS) ssNMR. The resonances >1200 ppm in Fig. 4f can be attributed to Li ions in TM layers, possessing mainly Li_1TM_5 and TM_6 local structures, respectively.[30–34] The resonances below 1200 ppm should be mainly assigned to the Li in Li layers and TM layers, but the high ppm region shows a different contribution from the Li in the Li layer in Li_2MnO_3 and NCM111. To quantify Li contents in TM layers, we calculated the area of resonances ≥ 1200 ppm and deduced the proportion in the whole range of 450–2000 ppm. As shown in Fig. 4g, the proportion increases with temperature. It may be correlated with the phase fusion. Correspondingly, we counted Li local structures containing 5 TMs and 6 TMs from these calculated structure models, and plotted the number as the phase fusion extent in Fig. 4h. It is clear that the proportion shows an increasing trend with the phase fusion extent. This means that the higher phase fusion extent will cause more Li local structures with TM_5 and TM_6, which is consistent with the ssNMR results in Fig. 4g.

Overall, the consistency between PDF results, ssNMR data and theoretical calculations provides irrefutable support for the higher phase fusion with temperature.

Understanding of phase fusion

The comprehensive experimental and theoretical results above can allow us to depict the whole process of two-phase fusion in the complicated LMR system from multiple angles in detail. As shown in Fig. 5a, the whole process can be divided into three stages: (1) the formation of two phases; (2) composite of two phases at the nanodomain scale; and (3) high-extent fusion of two phases at the atomic level. At the 1st stage, the Li_2MnO_3 phase and NCM111 phase formed into nearly core–shell particles at around 700 °C, which can be determined by the TM segregation detected by TEM–EDX and the phase compositions detected by SXRD. At the 2nd stage, two phases merge at the nanodomain scale above 800 °C, confirmed by the uniform elemental distribution by TEM–EDX, the phase boundaries observed in the HRTEM images of LLNCM-800, LLNCM-900, and LLNCM-1000, and the decreased FWHM values and peak shift of the main peaks in SXRD patterns. At the last stage, phase fusion reaches a higher extent and proceed among the different phase nanodomains, mainly through the TM migration and rearrangement in the TM layers of two layered phases, eventually to a nearly solid solution at 1100 °C, which can be evidenced by the shift of the TM–TM peak in PDF patterns from 1000 to 1100 °C, the changes in Li coordination environments observed in ssNMR, as well as the disappearance of grain boundaries in HRTEM images and TKD tests.

In the whole process of phase fusion, the O coordination environment could change with the phase fusion extent, which may affect the electrochemistry a lot.[35] To validate this deduction, the electrochemical performance of the five samples was evaluated in coin-type half cells. The initial charge/discharge curves are compared in Fig. 5b. The plateau above 4.45 V comes from lattice oxygen oxidation.[36] It is clear that the plateau becomes shorter with temperature, indicating that the contribution of oxygen redox to the capacity decreases with the phase fusion extent and the influence of synthesis method is excluded (Fig. S28 and S29, ESI†). When the phase fusion extent reached the maximum at 1100 °C, the O redox activity is sharply suppressed, indicated by the big capacity drop from 1000 to 1100 °C, which can be attributed to the dispersion of $LiMn_6$ superstructural units.[14,37,38] Fig. S30 (ESI†) illustrates that the band gap in the total density of states (DOS) narrows from 1.72 eV to 0.72 eV upon increasing the phase fusion degree. This reduction suggests an enhancement in electrical conductivity and potentially improved cycling performance.[39] Furthermore, the oxygen projected density of states (PDOS) show a notable decrease in band gap, indicating the oxygen is easier to be oxidized (Fig. S31, ESI†). Synchronous thermal analysis (TG-DSC) and phase diagram experiments were further performed to confirm the fusion ability at 1100 °C, demonstrating that interparticle elemental diffusion was achieved (Fig. S32 and S33, ESI†). This is significant because Li_2MnO_3 has traditionally been regarded as oxygen inert. However, upon sealing and sintering a tube of the material at 1100 °C for 1 hour, reversible oxygen activity was observed (Fig. S33c, ESI†). The results indicate that sintering at 1100 °C could affect the local structure and thus the oxygen redox chemistry. Therefore, the judgment of the phase fusion degree is valid above 900 °C. Multi-angle tracking oxygen behavior of phase evolution is needed to further understand the oxidation mechanism.[40–43] The long-cycling results show that the sample with the medium level of phase fusion has better electrochemical, structural stability and smaller voltage decay (Fig. 5c, Fig. S34 and S35, ESI†), which is consistent with our previous work.[14,37] Overall, LLNCM-1000 exhibits the best electrochemistry due to its balanced capacity and stability performance. Therefore, it is feasible to adjust the degree of phase fusion to achieve good cycling stability without sacrificing much O redox activity.

This direct correlation between phase fusion and temperature provides innovative approaches to designing new

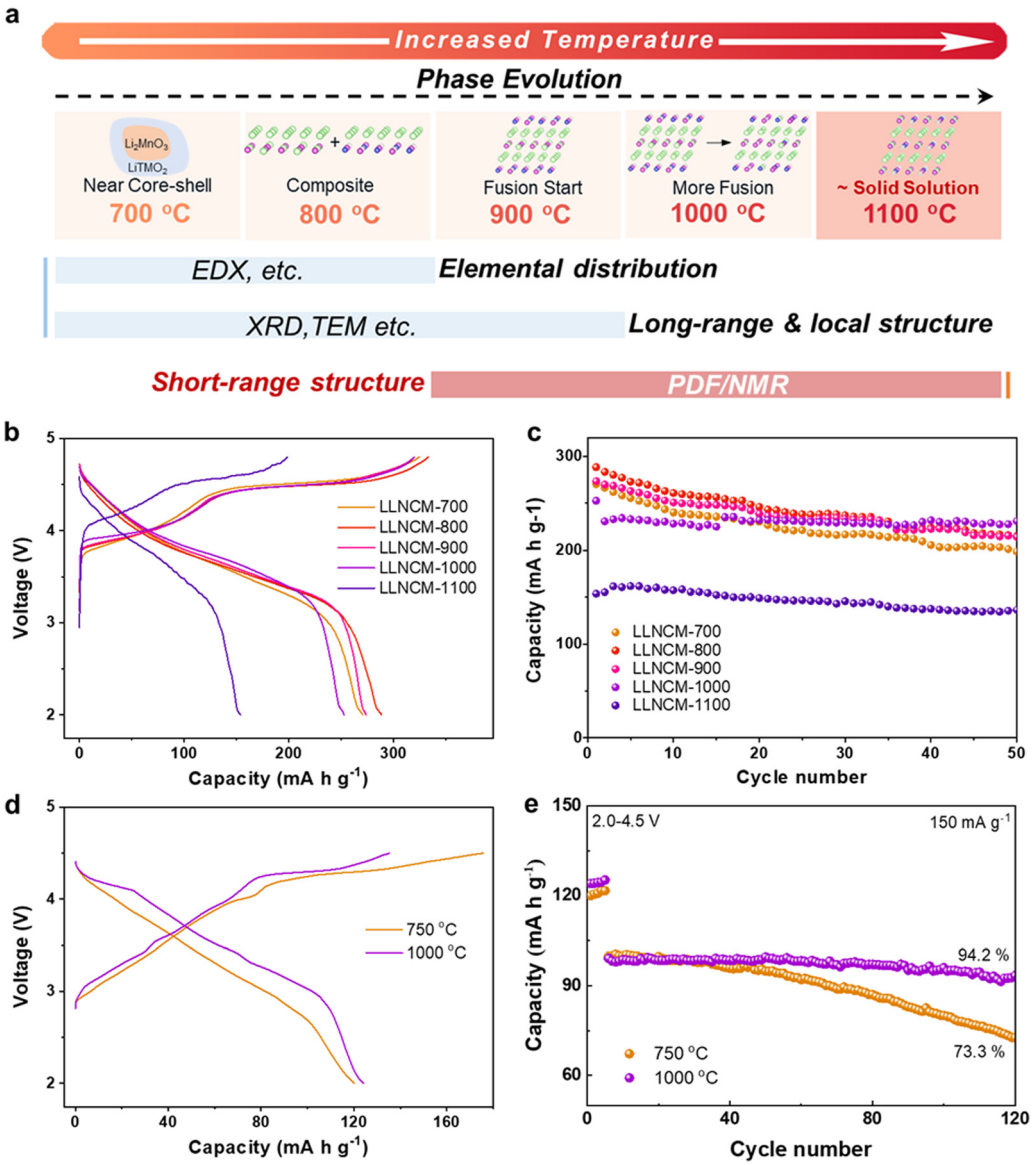

Fig. 5 The microscopic picture of phase fusion and the impact on electrochemical performance. (a) Mechanisms and pathways of phase evolution in Li-rich Mn-based cathodes. (b) Capacity–voltage profiles of LLNCM-700, LLNCM-800, LLNCM-900, LLNCM-1000 and LLNCM-1100 cathodes at the first cycle. (c) Cycling performance of different cathodes in the voltage range of 2–4.8 V at 0.1 C. (d) Capacity–voltage profiles of *C*2/*m* and *P*6$_3$*mmc* phases calcined at 750 °C and 1000 °C. (e) The corresponding electrochemical performance in the voltage range of 2.0–4.5 V at 1 C after 5 cycles' activation at 0.1 C.

materials. We further applied this phase fusion control strategy to Na-ion battery cathode composed of two layered phases (*C*2/*m* and *P*6$_3$*mmc*) (Fig. S36, ESI†). The medium degree of phase fusion successfully increased the capacity retention from 73% to 94% (Fig. 5d and e). Manipulating medium phase fusion in this manner is an effective way to optimize electrochemical performance, opening up new possibilities for advancing materials.

Conclusion

In summary, a thorough investigation was performed on the formation and fusion process of two extremely similar layered phases in Li-rich Mn-based cathode materials from different angles covering the elemental distribution, local structure, long-range structure, and short-range structure by employing a comprehensive multiscale characterization, including TEM–EDX, HRTEM, TKD, SXRD, PDF, and ssNMR. It clearly reveals the detailed process from the formation of two phases into different particles to two-phase merging into individual particles and eventually to phase fusion within individual particles at the atomic level. Importantly, synchrotron X-ray PDF analysis combined with theoretical calculations demonstrates for the first time that the TM–TM distance increases with the progress of the phase fusion, making it become an effective parameter for judging the extent of phase fusion. Furthermore, the cycling

stability was significantly enhanced without sacrificing the capacity by adjusting the phase fusion to a medium extent. This study provides a multiple technique integrated methodology to investigate the structural evolution in the complicated multiple phase system and also offers valuable insights into the design and optimization of complex layered cathodes by tuning the phase fusion extent.

Experimental section

Materials preparation

The precursor for $0.5Li[Li_{1/3}Mn_{2/3}]O{\cdot}0.5Li[Ni_{1/3}Co_{1/3}Mn_{1/3}]O_2$ (LLNCM) was obtained by a sol–gel method and a subsequent low-temperature sintering process. In a typical process, 4.9533 g $CH_3COOLi{\cdot}2H_2O$ (Aladdin, 99%, 3% excess), 1.6757 g $(CH_3COO)_2Ni{\cdot}4H_2O$ (Aladdin, 99%), 4.9513 g $(CH_3COO)_2Mn{\cdot}4H_2O$ (Aladdin, 99%) and 1.6773 g $(CH_3COO)_2Co{\cdot}4H_2O$ (Aladdin, 99.5%) in a stoichiometric ratio were mixed in 100 mL deionized water. 7.0047 g citric acid and 3.7137 g polyvinylpyrrolidone (Aladdin, K30) were added as the chelating agents. The solution was dried at 95 °C, and then the powder was calcined at 140 °C for 3 hours and 500 °C for 3 hours to obtain the precursor. The precursor was calcined at 700, 800, 900, 1000, and 1100 °C for 20, 15, 12, 10, and 6 hours, respectively, to obtain LLNCM-700, LLNCM-800, LLNCM-900, LLNCM-1000 and LLNCM-1100.

Materials characterization

The morphology (Fig. S1, ESI†) was characterized by scanning electron microscopy (SEM, ZEISS Supra 55 field emission scanning electron microscopy). The particle size distribution (Fig. S2, ESI†) was measured using a Nano-ZS90 zeta potential analyzer. Elemental composition (Table S1, ESI†) was analyzed using inductively coupled plasma-optical emission spectroscopy (ICP-OES, model: JY2000-2). The HRTEM and SAED images as well as EDX maps were taken using a JEOL-3200FS (FETEM, 300 kV). The atomic structures of the samples were analyzed using high-angle annular dark-field scanning transmission electron microscopy (HAADF-STEM) on a double Cs-corrected FEI Titan Themis G2 TEM, operating at 300 kV. TKD images were collected using a FIB (FEI Scios-ZEISS SUPRA® 55) equipped with an Oxford symmetry electron back-scattering diffraction (EBSD) detector. The TKD data were processed by using the Oxford AZtec and HKL CHANNEL 5 software. X-ray powder diffraction and total scattering data of the five samples were collected at sector 11-ID-C of the Advanced Photon Source (Argonne National Laboratory). The beam size is 0.5 mm × 0.5 mm and the wavelength is 0.1173 Å. *In situ* heating SXRD measurement at 1000 °C was performed at the same beamline. *In situ* heating XRD measurement at 800 and 900 °C was performed employing a high power Bruker D8-Advance diffractometer using Cu-Kα radiation at 50 kV and 100 mA. Rietveld refinement of SXRD patterns and peak fitting were carried out using TOPAS software packages. Rietveld refinement of PDFs was performed using PDFgui.[44] TG-DSC was carried out using MDTC-EQ-M05-01. The staking faults were refined using the FAULTS program. The two-phase reaction process was analyzed by differential scanning calorimetry (DSC, MDTC-EQ-M05-01).[26] The XANES and EXAFS analyses were performed at the BL11B beamline of the Shanghai Synchrotron Radiation Facility (SSRF). MAS NMR spectroscopy were performed on a 400 MHz Bruker ADVANCE III spectrometer at a ^{7}Li Larmor frequency of 155.51 MHz using a triple-resonance 1.9 mm MAS probe. Spectra were recorded using the projected magic-angle turning phase-adjusted sideband separation (pj-MATPASS) pulse sequence with a $\pi/2$ pulse length of 1.6 μs and a recycle delay of 50 ms.

Electrochemical tests

Coin-type (CR2032) half cells were assembled to perform the electrochemical measurements. Active materials, polyvinylidene fluoride (PVDF, Solvay® 5130) and carbon black (C45 Conductive Carbon Black, TIMCAL) in a weight ratio of 7 : 2 : 1 was mixed in *n*-methyl-2-pyrrolidone (NMP). The mixture was stirred at 2000 rpm for 9 min (THINKY AR-100) to form a uniform slurry, which was blade-casted on an Al foil and dried at 80 °C in a vacuum for 10 hours. 1.2 M $LiPF_6$ solution in EC/EMC (3 : 7) mixed solvent was used as the electrolyte. The galvanostatic charge–discharge tests were performed using a NEWARE battery testing system (MIHW-200-160CH, 1 C = 200 mA g^{-1}).

Theoretical calculations

All the density functional theory (DFT) calculations were executed using Vienna *ab initio* simulation package (VASP).[45] The Perdew–Burke–Ernzerhof (PBE) form of generalized gradient approximation (GGA) based on the projector-augmented wave (PAW) method is selected to describe the electronic exchange–correlation potential.[46–48] The cut-off energy for structural optimization and static electron energy calculations is 520 eV and the electronic energy convergence criterion is set at 10^{-5} eV. The conjugate gradient algorithm is used for ionic relaxation. To correctly characterize the localization of the TM d-electrons, the PBE+*U* method was used to account for the strong correlation interaction.[49,50] The short-range on-site Coulomb interactions (*U*) presented in the localized 3d electrons of Mn, Co and Ni are 4.2, 3.3 and 6.4 eV, respectively. The first Brillouin zone is sampled using a reciprocal 2 × 2 × 2 Monkhorst–Pack grid. The optimized residual force on each atom of geometries was less than 0.01 eV $Å^{-1}$. DFT-D3 semi-empirical van der Waals correction is applied for making up for the defects of DFT in dealing with the dispersion force during structural relaxation.[51] The spin-polarized calculations were considered in all our calculations. All calculations were performed considering a ferromagnetic ordering of transition metal atoms. Mn, Ni, and Co are ferromagnetic inside, and calculations consider antiferromagnetic between Mn and Ni.[52]

During the phase mixing process, the main source of configuration entropy is the distribution and component of metal ions (Li, Ni, Co, Mn) in transition metal layers. The no-fusion structure composed with Li_2MnO_3 and NCM111 has the

well-defined metal distribution. In the theoretically solid solution structure with the maximum degree of mixing, Li^+ and the transition metal ions are randomly arranged. Using the no-fusion structure and solid solution structure as the end members, the special quasi-random structure (SQS) models with medium-level and high-level phase fusion (mixing) can be constructed.

Author contributions

S. X., F. P. and M. Z. conceived the idea and designed the experiments. S. X. and W. R. synthesized all the materials and conducted the electrochemical measurements. S. X. designed the phase diagram related experiments. S. X., W. Z. and W. W. carried out the TEM, SAED, HADDF-STEM and TKD measurements. T. L. and S. X. performed *ex situ* synchrotron PDF, XRD and *in situ* heating XRD. B. H., X. L., H. L., M. Z. and S. X. performed ssNMR and data analysis. S. X., M. Z., C. Y., J. L., X. T., C. D. and F. P. performed the structural analysis and refinement. B. Q. and S. X. carried out the XANES and EXAFS. S. X., X. Y., Z. G., L. W. and Z. Y. performed the TG-DSC, ICP and SEM characterization. Z. C., C. H. and S. X. conducted the DFT calculations. S. X., F. P. and M. Z. wrote the manuscript and all authors edited the manuscript.

Conflicts of interest

There are no conflicts to declare.

Acknowledgements

This work was financially supported by the National Natural Science Foundation of China (52172175), the Shenzhen Science and Technology Research Grant (JCYJ20210324130812033), the Shenzhen Key Laboratory of Eco-materials and Renewable Energy (ZDSYS20200922160400001), the Program from Guangdong Introducing Innovative and Entrepreneurial Teams (2019ZT08L101 and RCTDPT-2020-001), the Basic and Applied Basic Research Foundation of Guangdong Province (No. 2021B1515130002) and the Chemistry and Chemical Engineering Guangdong Laboratory (1922018). This research used the resources of the Advanced Photon Source, a US Department of Energy (DOE) Office of Science User Facility operated for the DOE Office of Science by Argonne National Laboratory under contract no. DE-AC02-06CH11357.

Notes and references

1 P. K. Nayak, E. M. Erickson, F. Schipper, T. R. Penki, N. Munichandraiah, P. Adelhelm, H. Sclar, F. Amalraj, B. Markovsky and D. Aurbach, *Adv. Energy Mater.*, 2018, **8**, 1702397.

2 L. Y. Yang, K. Yang, J. X. Zheng, K. Xu, K. Amine and F. Pan, *Chem. Soc. Rev.*, 2020, **49**, 4667–4680.

3 M. H. Rossouw and M. M. Thackeray, *Mater. Res. Bull.*, 1991, **26**, 463–473.

4 F. Ning, B. Li, J. Song, Y. Zuo, H. Shang, Z. Zhao, Z. Yu, W. Chu, K. Zhang, G. Feng, X. Wang and D. Xia, *Nat. Commun.*, 2020, **11**, 4973.

5 A. Singer, M. Zhang, S. Hy, D. Cela, C. Fang, T. A. Wynn, B. Qiu, Y. Xia, Z. Liu, A. Ulvestad, N. Hua, J. Wingert, H. Liu, M. Sprung, A. V. Zozulya, E. Maxey, R. Harder, Y. S. Meng and O. G. Shpyrko, *Nat. Energy*, 2018, **3**, 641–647.

6 Y. Yang, Z. Zhang, S. Liu, B. Wang, J. Liu, Y. Ren, X. Zhang, S. Zhao, D. Liu and H. Yu, *Matter.*, 2022, **5**, 3869–3882.

7 F. Amalraj, D. Kovacheva, M. Talianker, L. Zeiri, J. Grinblat, N. Leifer, G. Goobes, B. Markovsky and D. Aurbach, *J. Electrochem. Soc.*, 2010, **157**, A1121.

8 Y. Lei, J. Ni, Z. Hu, Z. Wang, F. Gui, B. Li, P. Ming, C. Zhang, Y. Elias, D. Aurbach and Q. Xiao, *Adv. Energy Mater.*, 2020, **10**, 2002506.

9 A. Boulineau, L. Simonin, J.-F. Colin, E. Canévet, L. Daniel and S. Patoux, *Chem. Mater.*, 2012, **24**, 3558–3566.

10 H. Yu, H. Kim, Y. Wang, P. He, D. Asakura, Y. Nakamura and H. Zhou, *Phys. Chem. Chem. Phys.*, 2012, **14**, 6584–6595.

11 J. Bareño, C. H. Lei, J. G. Wen, S.-H. Kang, I. Petrov and D. P. Abraham, *Adv. Mater.*, 2010, **22**, 1122–1127.

12 E. McCalla, A. W. Rowe, J. Camardese and J. R. Dahn, *Chem. Mater.*, 2013, **25**, 2716–2721.

13 Z. Lu and J. R. Dahn, *J. Electrochem. Soc.*, 2002, **149**, A815.

14 Y. Li, S. Xu, W. Zhao, Z. Chen, Z. Chen, S. Li, J. Hu, B. Cao, J. Li, S. Zheng, Z. Chen, T. Zhang, M. Zhang and F. Pan, *Energy Storage Mater.*, 2022, **45**, 422–431.

15 T. Liu, J. Liu, L. Li, L. Yu, J. Diao, T. Zhou, S. Li, A. Dai, W. Zhao, S. Xu, Y. Ren, L. Wang, T. Wu, R. Qi, Y. Xiao, J. Zheng, W. Cha, R. Harder, I. Robinson, J. Wen, J. Lu, F. Pan and K. Amine, *Nature*, 2022, **606**, 305–312.

16 F. Lin, D. Nordlund, T. C. Weng, Y. Zhu, C. Ban, R. M. Richards and H. L. Xin, *Nat. Commun.*, 2014, **5**, 3358.

17 R. Lin, E. Hu, M. Liu, Y. Wang, H. Cheng, J. Wu, J. C. Zheng, Q. Wu, S. Bak, X. Tong, R. Zhang, W. Yang, K. A. Persson, X. Yu, X. Q. Yang and H. L. Xin, *Nat. Commun.*, 2019, **10**, 1650.

18 L. Wang, T. Liu, A. Dai, V. De Andrade, Y. Ren, W. Xu, S. Lee, Q. Zhang, L. Gu, S. Wang, T. Wu, H. Jin and J. Lu, *Nat. Commun.*, 2021, **12**, 5370.

19 N. Guerrini, L. Jin, J. G. Lozano, K. Luo, A. Sobkowiak, K. Tsuruta, F. Massel, L.-C. Duda, M. R. Roberts and P. G. Bruce, *Chem. Mater.*, 2020, **32**, 3733–3740.

20 P. Yan, L. Xiao, J. Zheng, Y. Zhou, Y. He, X. Zu, S. X. Mao, J. Xiao, F. Gao, J.-G. Zhang and C.-M. Wang, *Chem. Mater.*, 2015, **27**, 975–982.

21 T. Matsunaga, H. Komatsu, K. Shimoda, T. Minato, M. Yonemura, T. Kamiyama, S. Kobayashi, T. Kato, T. Hirayama, Y. Ikuhara, H. Arai, Y. Ukyo, Y. Uchimoto and Z. Ogumi, *Chem. Mater.*, 2016, **28**, 4143–4150.

22 X. Liu, G.-L. Xu, V. S. C. Kolluru, C. Zhao, Q. Li, X. Zhou, Y. Liu, L. Yin, Z. Zhuo, A. Daali, J.-J. Fan, W. Liu, Y. Ren, W. Xu, J. Deng, I. Hwang, D. Ren, X. Feng, C. Sun, L. Huang, T. Zhou, M. Du, Z. Chen, S.-G. Sun, M. K. Y. Chan, W. Yang, M. Ouyang and K. Amine, *Nat. Energy*, 2022, **7**, 808–817.

23 D. Q. Liu, Z. Shadike, R. Q. Lin, K. Qian, H. Li, K. K. Li, S. W. Wang, Q. P. Yu, M. Liu, S. Ganapathy, X. Y. Qin, Q. H. Yang, M. Wagemaker, F. Y. Kang, X. Q. Yang and B. H. Li, *Adv. Mater.*, 2019, **31**, 1806620.
24 X. Wang, Q. Zhang, C. Zhao, H. Li, B. Zhang, G. Zeng, Y. Tang, Z. Huang, I. Hwang, H. Zhang, S. Zhou, Y. Qiu, Y. Xiao, J. Cabana, C.-J. Sun, K. Amine, Y. Sun, Q. Wang, G.-L. Xu, L. Gu, Y. Qiao and S.-G. Sun, *Nat. Energy*, 2024, **9**, 184–196.
25 Y. Tang, Q. Zhang, W. Zuo, S. Zhou, G. Zeng, B. Zhang, H. Zhang, Z. Huang, L. Zheng, J. Xu, W. Yin, Y. Qiu, Y. Xiao, Q. Zhang, T. Zhao, H.-G. Liao, I. Hwang, C.-J. Sun, K. Amine, Q. Wang, Y. Sun, G.-L. Xu, L. Gu, Y. Qiao and S.-G. Sun, *Nat. Sustainability*, 2024, **7**, 348–359.
26 R. Shunmugasundaram, R. S. Arumugam and J. R. Dahn, *J. Electrochem. Soc.*, 2016, **163**, A1394–A1400.
27 B. Li, Z. Zhuo, L. Zhang, A. Iadecola, X. Gao, J. Guo, W. Yang, A. V. Morozov, A. M. Abakumov and J. M. Tarascon, *Nat. Mater.*, 2023, **22**, 1370–1379.
28 Y. He, Y. Zhang, Z. Wang, X. Li, Z. Lü, X. Huang and Z. Liu, *Adv. Funct. Mater.*, 2021, **31**, 2101737.
29 S.-J. Hwang, H.-S. Park, J.-H. Choy and G. Campet, *J. Phys. Chem. B*, 2001, **105**, 335–342.
30 F. Dogan, J. R. Croy, M. Balasubramanian, M. D. Slater, H. Iddir, C. S. Johnson, J. T. Vaughey and B. Key, *J. Electrochem. Soc.*, 2014, **162**, A235–A243.
31 F. Dogan, B. R. Long, J. R. Croy, K. G. Gallagher, H. Iddir, J. T. Russell, M. Balasubramanian and B. Key, *J. Am. Chem. Soc.*, 2015, **137**, 2328–2335.
32 X. Liu, Z. Liang, Y. Xiang, M. Lin, Q. Li, Z. Liu, G. Zhong, R. Fu and Y. Yang, *Adv. Mater.*, 2021, **33**, e2005878.
33 O. Pecher, J. Carretero-González, K. J. Griffith and C. P. Grey, *Chem. Mater.*, 2016, **29**, 213–242.
34 Y. Xiang, X. Li, Y. Cheng, X. Sun and Y. Yang, *Mater. Today*, 2020, **36**, 139–157.
35 D. H. Seo, J. Lee, A. Urban, R. Malik, S. Kang and G. Ceder, *Nat. Chem.*, 2016, **8**, 692–697.
36 S. Zhao, K. Yan, J. Zhang, B. Sun and G. Wang, *Angew. Chem., Int. Ed.*, 2021, **60**, 2208–2220.
37 W. Huang, C. Lin, J. Qiu, S. Li, Z. Chen, H. Chen, W. Zhao, G. Ren, X. Li, M. Zhang and F. Pan, *Chem*, 2022, **8**, 2163–2178.
38 Z. Li, Y. Li, M. Zhang, Z. W. Yin, L. Yin, S. Xu, C. Zuo, R. Qi, H. Xue, J. Hu, B. Cao, M. Chu, W. Zhao, Y. Ren, L. Xie, G. Ren and F. Pan, *Adv. Energy Mater.*, 2021, **11**, 2101962.
39 S. Xu, X. Tan, W. Ding, W. Ren, Q. Zhao, W. Huang, J. Liu, R. Qi, Y. Zhang, J. Yang, C. Zuo, H. Ji, H. Ren, B. Cao, H. Xue, Z. Gao, H. Yi, W. Zhao, Y. Xiao, Q. Zhao, M. Zhang and F. Pan, *Angew. Chem., Int. Ed.*, 2023, **62**, e202218595.
40 X. Wu, H. Liu, X. Lou, F. Geng, J. Li, C. Li and B. Hu, *J. Phys. Chem. Lett.*, 2023, **14**, 7711–7717.
41 R. A. House, G. J. Rees, M. A. Pérez-Osorio, J.-J. Marie, E. Boivin, A. W. Robertson, A. Nag, M. Garcia-Fernandez, K.-J. Zhou and P. G. Bruce, *Nat. Energy*, 2020, **5**, 777–785.
42 R. A. House, H. Y. Playford, R. I. Smith, J. Holter, I. Griffiths, K.-J. Zhou and P. G. Bruce, *Energy Environ. Sci.*, 2022, **15**, 376–383.
43 P. M. Csernica, S. S. Kalirai, W. E. Gent, K. Lim, Y.-S. Yu, Y. Liu, S.-J. Ahn, E. Kaeli, X. Xu, K. H. Stone, A. F. Marshall, R. Sinclair, D. A. Shapiro, M. F. Toney and W. C. Chueh, *Nat. Energy*, 2021, **6**, 642–652.
44 C. Farrow, P. Juhas, J. Liu, D. Bryndin, E. Božin, J. Bloch, T. Proffen and S. Billinge, *J. Phys.: Condens. Matter*, 2007, **19**, 335219.
45 G. Kresse and J. Hafner, *Phys. Rev. B: Condens. Matter Mater. Phys.*, 1993, **47**, 558–561.
46 G. Kresse and D. Joubert, *Phys. Rev. B: Condens. Matter Mater. Phys.*, 1999, **59**, 1758–1775.
47 P. E. Blöchl, *Phys. Rev. B: Condens. Matter Mater. Phys.*, 1994, **50**, 17953–17979.
48 J. P. Perdew, K. Burke and M. Ernzerhof, *Phys. Rev. Lett.*, 1996, **77**, 3865–3868.
49 S. L. Dudarev, G. A. Botton, S. Y. Savrasov, C. J. Humphreys and A. P. Sutton, *Phys. Rev. B: Condens. Matter Mater. Phys.*, 1998, **57**, 1505–1509.
50 V. I. Anisimov, J. Zaanen and O. K. Andersen, *Phys. Rev. B: Condens. Matter Mater. Phys.*, 1991, **44**, 943–954.
51 S. Grimme, J. Antony, S. Ehrlich and H. Krieg, *J. Chem. Phys.*, 2010, **132**, 154104.
52 S. Q. Wu, Z. Z. Zhu, Y. Yang and Z. F. Hou, *Comput. Mater. Sci.*, 2009, **44**, 1243–1251.

